

Lattice dynamics and spontaneous magnetodielectric effect in ilmenite CoTiO_3

R. M. Dubrovin^{a,*}, N. V. Siverin^a, M. A. Prosnikov^{b,c}, V. A. Chernyshev^d, N. N. Novikova^e, P. C. M. Christianen^{b,c}, A. M. Balbashov^f and R. V. Pisarev^a

^aIoffe Institute, Russian Academy of Sciences, 194021 St.-Petersburg, Russia

^bHigh Field Magnet Laboratory (HFML - EMFL), Radboud University, Toernooiveld 7, 6525 ED Nijmegen, The Netherlands

^cRadboud University, Institute for Molecules and Materials, Heyendaalseweg 135, 6525 AJ Nijmegen, The Netherlands

^dDepartment of Basic and Applied Physics, Ural Federal University, 620002 Ekaterinburg, Russia

^eInstitute of Spectroscopy, Russian Academy of Sciences, 108840 Moscow, Troitsk, Russia

^fMoscow Power Engineering Institute, 111250 Moscow, Russia

ARTICLE INFO

Keywords:

CoTiO_3

Ilmenite

Single crystals

Lattice dynamics

Infrared spectroscopy

Raman spectroscopy

Dielectric spectroscopy

DFT calculations

ABSTRACT

Ilmenite-type crystals find a variety of technological applications due to their intriguing physical properties. We present the results of the lattice dynamics studies of honeycomb antiferromagnetic ilmenite CoTiO_3 single crystal by the complementary polarized infrared, Raman, and dielectric spectroscopic techniques that are supplemented by the DFT calculations. The frequencies and symmetries of all predicted infrared and Raman active phonons were uniquely identified. Furthermore, it was found that the dielectric permittivity demonstrates distinct changes below antiferromagnetic ordering temperature in zero magnetic field due to spontaneous magnetodielectric effect. Our results establish the reliable basis for further investigation of the coupling of phonons with spins, magnetic excitations and other physical phenomena of this promising material.

1. Introduction

Titanate materials ATiO_3 have an astonishing variety of different crystal structures depending on the chemical composition, which is manifested in numerous intriguing physical phenomena such as ferroelectricity, magnetism, multiferroicity, piezoelectricity, and some others [1]. Among them, cobalt titanate CoTiO_3 , which possesses a very stable ilmenite structure in a wide range of temperatures and pressures [2], has numerous successful industrial applications such as high- κ dielectric [3], resonator antenna [4], catalysts [5, 6, 7], gas sensors [8, 9], a potential anode material for Li-ion batteries [10, 11, 12, 13]. From the condensed matter physics point of view the CoTiO_3 exhibits exciting phenomena, e.g., Dirac magnons [14, 15] and magnetodielectric coupling [16] whereas isostructural MnTiO_3 reveals linear magnetoelectric effect [17, 18] and magnetochiral dichroism [19]. But further intensive research of this promising material is inhibited by the lack of complete information about the phonon spectrum. It is worth noting that up to now, most experimental studies of the lattice dynamics of ATiO_3 materials with ilmenite structure were performed on the poly- and microcrystalline samples using unpolarized far infrared [20, 21, 22, 23, 24, 25] and Raman [26, 27, 28, 29, 30, 31, 32, 33] spectroscopy.


In this paper, we present results on the lattice dynamics study of CoTiO_3 single crystal with ilmenite structure us-

ing complementary dielectric, far-infrared reflectivity, and Raman scattering polarized spectroscopic techniques. Obtained experimental results, supplemented by the lattice dynamics calculations, allowed us to determine the frequencies and symmetries of infrared and Raman active phonons. Moreover, we show that the antiferromagnetic ordering leads to notable changes in the dielectric permittivity in zero magnetic field due to the spontaneous magnetodielectric effect.

2. Experimental and Computational Details

The CoTiO_3 single crystal was grown by floating zone melting method with light heating in oxygen flow using polycrystalline powder synthesized with Co_3O_4 and TiO_2 of 4N purity as describes in details in Ref. [34]. The X-ray oriented single crystal was cut close to normal to the hexagonal a and c axes and optically polished. The far-infrared reflectivity measurements were carried out using Fourier-transform IR spectrometer Bruker IFS 66v/S in the spectral range of 50–7500 cm^{-1} at room temperature. Raman scattering spectra were measured in the range 15–1200 cm^{-1} with the use of FHR1000 (HORIBA) monochromator equipped by 1200 lines/mm grating, 100 μm entrance slit, liquid nitrogen cooled PyLoN CCD camera (Princeton Instruments) and 660 nm excitation laser (Torus, LaserQuantum). Low excitation power of 500 μW was used to avoid the overheating of an optically dense sample. Electric measurements of dielectric permittivity were done using precision RLC meter AKTAKOM AM-3028 in the frequency range from 20 Hz to 1 MHz. Electric contacts were deposited on the sample faces using silver paint to form a capacitor. Measurements were performed in helium flow cryostat Cryo CRC 102 in the temperature range from 5 to 400 K at continuous heating.

*Corresponding author

 dubrovin@mail.ioffe.ru (R. M. Dubrovin)

ORCID(s): 0000-0002-7235-7805 (R. M. Dubrovin);

0000-0002-4643-845X (N. V. Siverin); 0000-0002-7107-570X (

M. A. Prosnikov); 0000-0002-3106-3069 (V. A. Chernyshev);

0000-0003-2428-6114 (N. N. Novikova); 0000-0002-2008-9335 (

R. V. Pisarev)

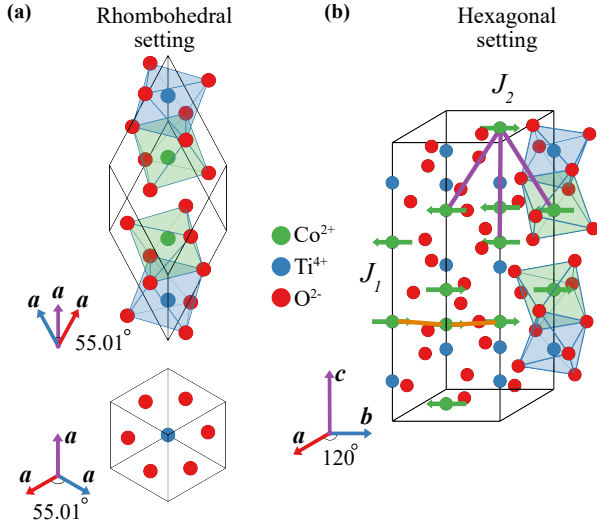


Figure 1: Crystal structure of ilmenite CoTiO_3 with trigonal space group $R\bar{3}$ in the (a) rhombohedral and (b) hexagonal settings. The orange and purple lines indicate the principal superexchange interaction J_1 and J_2 , respectively. Pictures were prepared using the VESTA software [42].

The measurements were complemented by lattice dynamical simulations which were performed according to the density functional theory (DFT) with the B3LYP hybrid functional [35] implemented on CRYSTAL14 package [36]. All-electron basis sets TZVP [37] for Co, 8-6411(31d)G [38] for Ti, and 8-411(1d)G [38] for O have been used according to Ref. [25]. The reciprocal space integration was performed by sampling the Brillouin zone with the $12 \times 12 \times 12$ Pack-Monkhorst k mesh. Coulomb and exchange integral tolerance factors were set to tight values of 10^{-8} , 10^{-8} , 10^{-8} , 10^{-9} , and 10^{-30} . The optimization of crystal structure was carried out and the experimental lattice parameters from Ref. [34] were well reproduced with an error of about 1.2%. The phonon spectrum was calculated by means of numerical second derivatives of the total energy as described in Ref. [39]. The static dielectric tensor, Born effective charges and phonon intensities were calculated using the CPHF/KS approach [40, 41].

3. Results and Discussion

CoTiO_3 has an ilmenite crystal structure with trigonal space group $R\bar{3}$ (C_{3i}^2 , #148, $Z = 2$ in rhombohedral and $Z = 6$ in hexagonal cell). The structure is formed by altering layers of corner sharing CoO_6 and TiO_6 octahedra, alternately stacked along the c axis in the hexagonal settings as shown in Fig. 1 [43]. The lattice parameters at room temperature are $a = 5.4846 \text{ \AA}$, $\theta = 55.01^\circ$ in rhombohedral setting and $a = b = 5.056$, $c = 13.91 \text{ \AA}$ in hexagonal setting, as shown in Figs. 1a and b, respectively [43, 44, 16, 34]. The hexagonal setting will be used throughout the paper below. The unit cell contains 30 ions occupying the Wyckoff positions $6c$ (0, 0, 0.3551) for Co^{2+} , $6c$ (0, 0, 0.1456) for Ti^{4+} , and $18f$ (0.3162, 0.0209, 0.2459) for O^{2-} as shown in

Fig. 1b. Below the Néel temperature $T_N = 38 \text{ K}$, the $S = \frac{3}{2}$ spins of Co^{2+} ($3d^7$) ions, form ferromagnetic honeycomb ab planes which are antiferromagnetically coupled along the c axis [43, 14], as can be seen in Fig. 1b.

The group-theoretical analysis for the ilmenite CoTiO_3 predicts 20 phonons [45]

$$\Gamma_{\text{total}} = 5A_g \oplus 5E_g \oplus 5A_u \oplus 5E_u, \quad (1)$$

among which there are 2 acoustic $\Gamma_{\text{acoustic}} = A_u \oplus E_u$, 8 infrared active $\Gamma_{\text{IR}} = 4A_u \oplus 4E_u$, and 10 Raman active $\Gamma_{\text{Raman}} = 5A_g \oplus 5E_g$ phonons, where A and E are non-degenerate and doubly degenerate modes, respectively.

3.1. Far-infrared reflectivity

Figure 2 shows the far-infrared reflectivity spectra of the ilmenite CoTiO_3 with polarization of light along the hexagonal axes at room temperature. These reflectivity spectra are very similar to observed in the isostructural natural FeTiO_3 crystal [23]. Four well-resolved bands in accordance with the symmetry prediction were detected for the both polarizations. Reflectivity spectra were analyzed using the generalized oscillator model of complex dielectric function [46]

$$\varepsilon(\omega) = \varepsilon_1(\omega) - i\varepsilon_2(\omega) = \varepsilon_\infty \prod_j \frac{\omega_{j\text{LO}}^2 - \omega^2 + i\gamma_{j\text{LO}}\omega}{\omega_{j\text{TO}}^2 - \omega^2 + i\gamma_{j\text{TO}}\omega}, \quad (2)$$

where ε_∞ is the high-frequency dielectric permittivity due to the electronic polarization contribution, $\omega_{j\text{LO}}$, $\omega_{j\text{TO}}$, $\gamma_{j\text{LO}}$ and $\gamma_{j\text{TO}}$ correspond to longitudinal LO and transverse TO frequencies and dampings of j th infrared active phonon, respectively. N is the number of polar phonons. At near normal incidence, the reflectivity R is related to the complex dielectric function by the Fresnel equation [47]

$$R(\omega) = \left| \frac{\sqrt{\varepsilon(\omega)} - 1}{\sqrt{\varepsilon(\omega)} + 1} \right|^2. \quad (3)$$

Results of fits of experimental data using Eqs. (2) and (3) are shown by black curves in Figs. 2a and b. There is a good agreement between experimental data and fits. The spectra of real ε_1 and imaginary ε_2 parts of complex dielectric function $\varepsilon = \varepsilon_1 - i\varepsilon_2$ calculated using obtained fit parameters are shown in Figs. 2c and d.

Parameters of all predicted $4A_u$ and $4E_u$ polar phonons were reliably determined from the fits of experimental data and are listed in Table 1. There is a qualitative agreement between experimental and literature phonon frequencies received from powder CoTiO_3 sample [20]. Obtained TO and LO phonon frequencies allow us to calculate the dielectric strength $\Delta\varepsilon_j$ of a j th phonon using an expression [48]

$$\Delta\varepsilon_j = \frac{\varepsilon_\infty}{\omega_{j\text{TO}}^2} \frac{\prod_k \omega_{k\text{LO}}^2 - \omega_{j\text{TO}}^2}{\prod_{k \neq j} \omega_{k\text{TO}}^2 - \omega_{j\text{TO}}^2}. \quad (4)$$

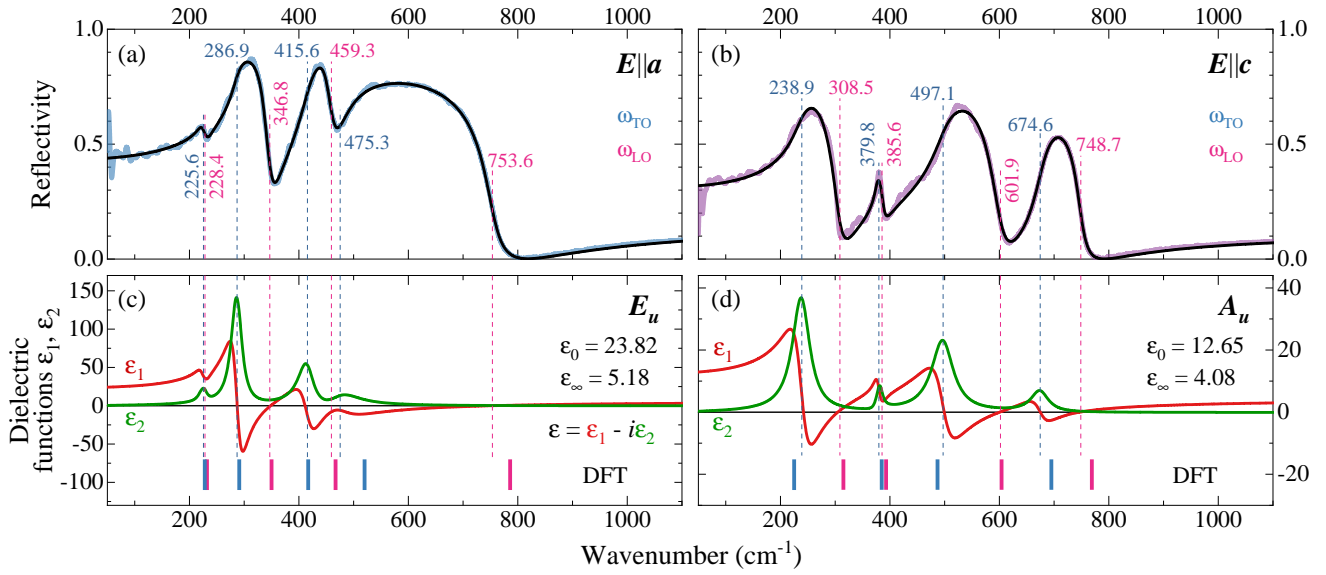


Figure 2: Far-infrared reflectivity spectra of CoTiO₃ at room temperature with the electric field of light E polarized along (a) the a axis and (b) the c axis. The black lines are results of fits based on a generalized oscillator model according to Eq. (2). Spectra of real ϵ_1 and imaginary ϵ_2 parts of the complex dielectric function ϵ for (c) A_u and (d) E_u phonons, corresponding to the fits. Blue and magenta vertical dashed lines correspond to ω_{TO} and ω_{LO} phonon frequencies obtained from the fit, respectively. The experimental values of the static ϵ_0 and high-frequency ϵ_∞ dielectric permittivities are given. Sticks in the lower parts of the (c) and (d) panels present the calculated phonon frequencies.

Table 1

Parameters of the IR active phonons in CoTiO₃ at room temperature: frequencies ω_j (cm⁻¹), dampings γ_j (cm⁻¹), and dielectric strengths $\Delta\epsilon_j$. The results of DFT calculations are presented in parenthesis.

Sym.	j	ω_{jTO}	γ_{jTO}	ω_{jLO}	γ_{jLO}	$\Delta\epsilon_j$
E_u	1	225.6 (228)	12.3	228.4 (232)	11.8	1.11 (1.39)
	2	286.9 (291)	20.7	346.8 (350)	23.4	11.03 (9.3)
	3	415.6 (417)	33.4	459.3 (467)	27.3	4.9 (3.41)
	4	475.3 (520)	66.5	753.6 (786)	34.3	1.61 (2.83)
			$\epsilon_0^{\text{opt}} = 23.83$ (22.07)		$\epsilon_\infty = 5.18$ (5.14)	
A_u	1	238.9 (225)	36.9	308.5 (315)	28.7	5.82 (9.16)
	2	379.8 (385)	8.5	385.6 (393)	13.4	0.2 (0.29)
	3	497.1 (487)	46.6	601.9 (604)	38.3	2.19 (2.27)
	4	674.6 (695)	36.7	748.7 (769)	20.2	0.38 (0.4)
			$\epsilon_0^{\text{opt}} = 12.67$ (16.38)		$\epsilon_\infty = 4.08$ (4.26)	

The optical static dielectric permittivity ϵ_0^{opt} can be obtained by adding the dielectric strengths over all polar phonons according to expression

$$\epsilon_0^{\text{opt}} = \epsilon_\infty + \sum_j^N \Delta\epsilon_j. \quad (5)$$

Values of the $\Delta\epsilon_j$ for all polar phonons and ϵ_0^{opt} are listed in Table 1. It is worth noting that, in CoTiO₃ the values of ϵ_0^{opt} along the a and c axes differ by about 2 times indicating strong anisotropy of the dielectric permittivity. Moreover, the high-frequency dielectric permittivity ϵ_∞ is also significantly different for the main crystallographic axes, as shown in Figs. 2a and b.

We performed the DFT calculations of lattice dynamics at the Brillouin zone center of the ilmenite CoTiO₃. The obtained TO and LO frequencies of the polar phonons are given in parenthesis in Table 1 and are shown by sticks in Figs. 2c and d. The experimental phonon frequencies are slightly less than calculated due to the anharmonic effects appearing at room temperature [49]. Nevertheless, there is a good agreement between experimental and calculated results. Furthermore, the strong anisotropy of ϵ_0^{opt} and ϵ_∞ dielectric permittivity were also well reproduced in our computations. We add that a strong dielectric anisotropy has been theoretically predicted for isostructural FeTiO₃ [50] and MgTiO₃ [51] and experimentally observed in CdTiO₃ [25] ilmenite crystals.

The DFT calculations also provide the normal mode eigen-

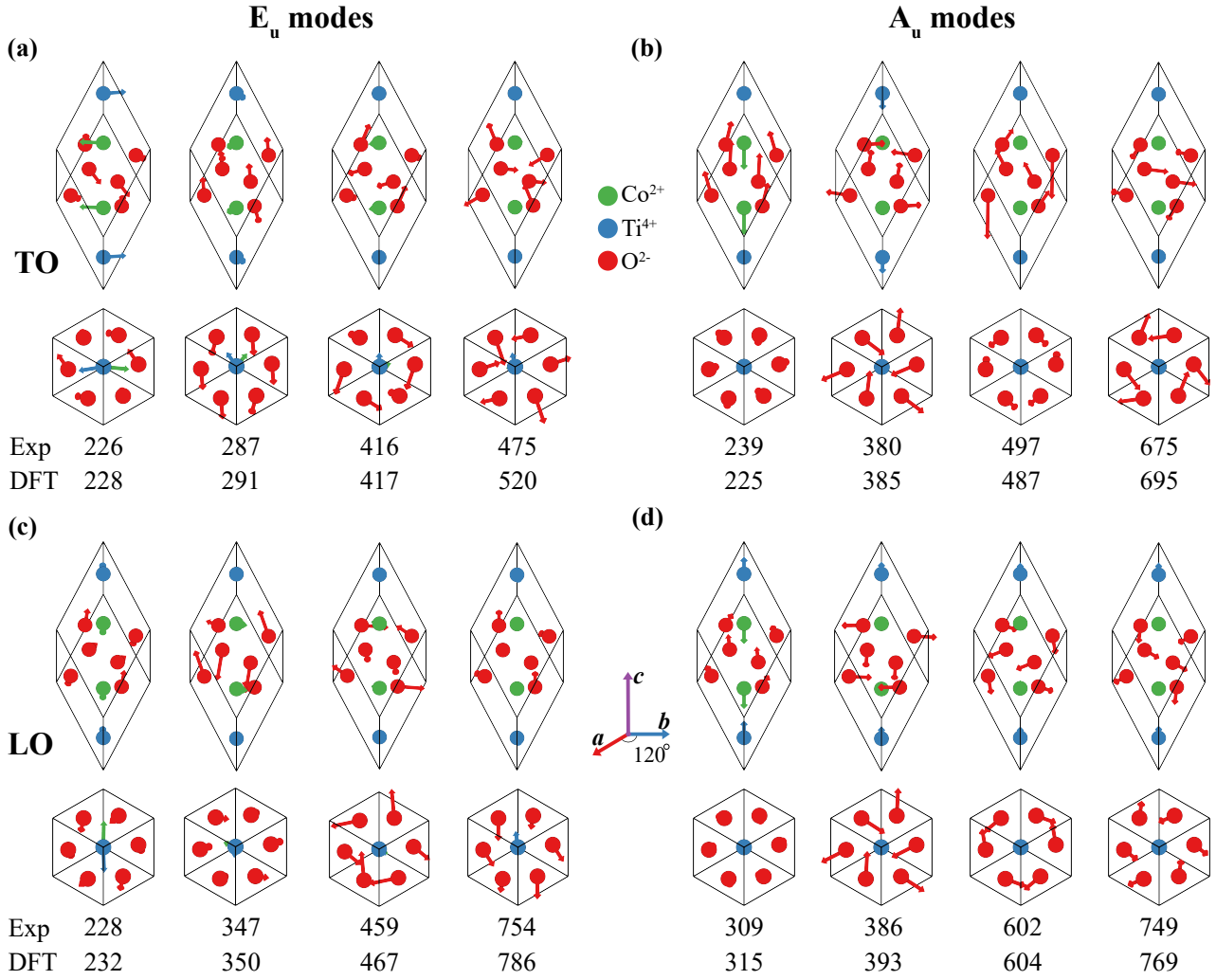


Figure 3: Schematic representation of ionic displacements in the Brillouin zone center in CoTiO_3 for polar (a,c) $4E_u$ and (b,d) $4A_u$ TO and LO phonons in the two projections according to the DFT calculations. For clarity, the crystallographic axes are shown for the hexagonal setting. The relative amplitudes of vibrations are illustrated by arrows. The experimental and calculated values of phonon frequencies (cm^{-1}) are given.

vectors for ions. Figure 3 shows obtained ionic displacement patterns for all infrared active $4E_u$ and $4A_u$ phonons in ilmenite CoTiO_3 . It was found that the TO and LO modes of the E_u symmetry are related to the ab plane vibrations of Co and Ti ions, as can be seen in Figs. 3a and c, respectively. Whereas the A_u phonons mainly represent the vibrations of Co and Ti ions along the c axis for both TO and LO modes (see Figs. 3b and d). For all infrared active phonons the movements of oxygen anions correspond to the asymmetric breathing. It is worth noting that the calculated pattern of vibrational eigenvectors in ilmenite CoTiO_3 are close to the data for isostructural CdTiO_3 [25] and MgTiO_3 [24].

Figure 4 shows as stacked bar graphs the calculated average displacement of ions for $4E_u \oplus 4A_u$ infrared (left panels) and $5E_g \oplus 5A_g$ Raman (right panels) active phonon modes. For E_u and A_u modes, the displacements of Co ions are significant only for low-frequency phonons as can be seen on the left panel in Fig. 4. Apparently, this is due to the fact that Co is the heaviest ion in this crystal. The average am-

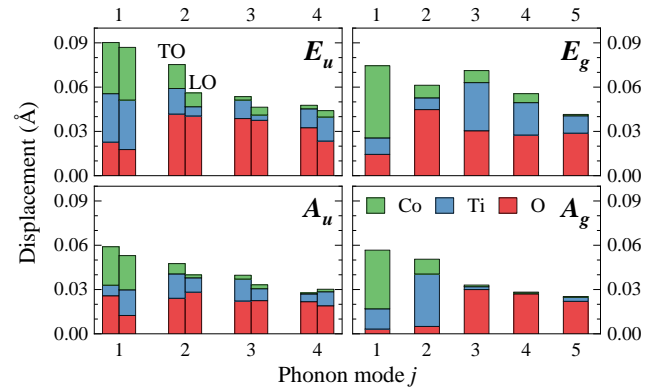


Figure 4: Average displacements of ions for infrared ($4E_u \oplus 4A_u$) and Raman ($5E_g \oplus 5A_g$) active phonon modes in ilmenite CoTiO_3 according to the DFT calculations.

plitudes of Ti and O ion vibrations are depend on phonon modes more weakly. For some phonons, there is a signif-

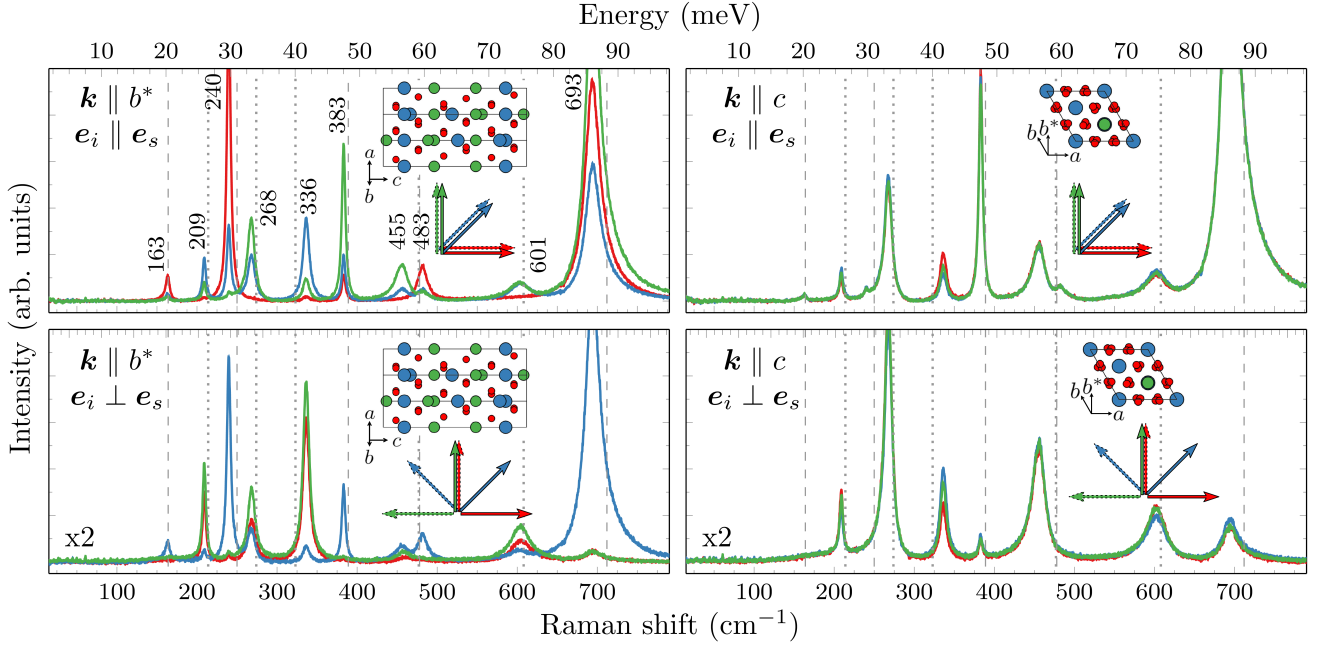


Figure 5: Raman scattering spectra of CoTiO₃ at room temperature. Linear background and weak quasielastic tail are subtracted. Insets show crystal structure projections in the ac - and ab -planes in left and right plots, respectively. Arrows represent the polarization of incident (e_i , solid outline) and scattered (e_s , dashed outline) light with respect to the crystallographic axes. The intensity of bottom plots is scaled by $\times 2$ to compensate weaker scattering in crossed polarizations. Vertical dashed and dotted lines correspond to calculated frequencies for A_g and E_g phonons, respectively. Numbers represent frequencies of the corresponding phonon modes.

icant difference in average displacements between TO and LO modes. Thus, for E_u phonons with $j = 2$ and 3 the amplitudes of Ti displacements for the TO modes are much larger than for the LO modes.

3.2. Raman scattering

Raman scattering is a powerful technique allowing observation of different types of even excitations. As suggested in Ref. [14] Raman technique could be applied for observation of bulk and surface magnons deep in the antiferromagnetic phase of CoTiO₃, however the reliable assignment of the bulk lattice modes is required beforehand. There are a few reports on Raman scattering studies of CoTiO₃, however they all were done on powder [28] and polycrystalline samples [31], which do not allow definitive determination of the phonon symmetries.

CoTiO₃ is a challenging crystal for Raman measurements due to its high optical density leading to poor scattering efficiency and unavoidable overheating. These restrictions can be avoided by choosing appropriate excitation line corresponding to one of the transparency windows. Two sets of spectra were recorded in the ac and ab planes, respectively, with the light linearly polarized along principal crystal axes, as well as for some intermediate directions, as shown in insets in Fig. 5. As expected, the A_g modes are isotropic in the ab plane, while showing considerable intensity difference in ac plane, according to scattering tensors Eq. (6) suggesting considerable difference in the a and b tensor elements for all

modes.

$$A_g = \begin{pmatrix} a & 0 & 0 \\ 0 & a & 0 \\ 0 & 0 & b \end{pmatrix}, \quad E_g = \begin{pmatrix} c & d & e \\ d & -c & f \\ e & f & 0 \end{pmatrix} \quad (6)$$

Table 2

Phonon frequencies (cm⁻¹) in comparison with results of DFT calculations, shown in parentheses. Full width at half maxima (FWHM, cm⁻¹) measured for polarization where the corresponding mode is strongest.

Symmetry	Mode	Frequency	FWHM
E_g	1	209 (214)	5.7
	2	268 (273)	11.2
	3	336 (323)	10.3
	4	455 (474)	20.9
	5	601 (608)	32.0
A_g	1	163 (164)	6.8
	2	240 (250)	6.7
	3	383 (389)	6.4
	4	483 (477)	15.8
	5	693 (712)	25.0

Small leakage of phonon modes is expected due to the light depolarization on optical elements and minor misalignment of the sample axes with respect to the light polarization.

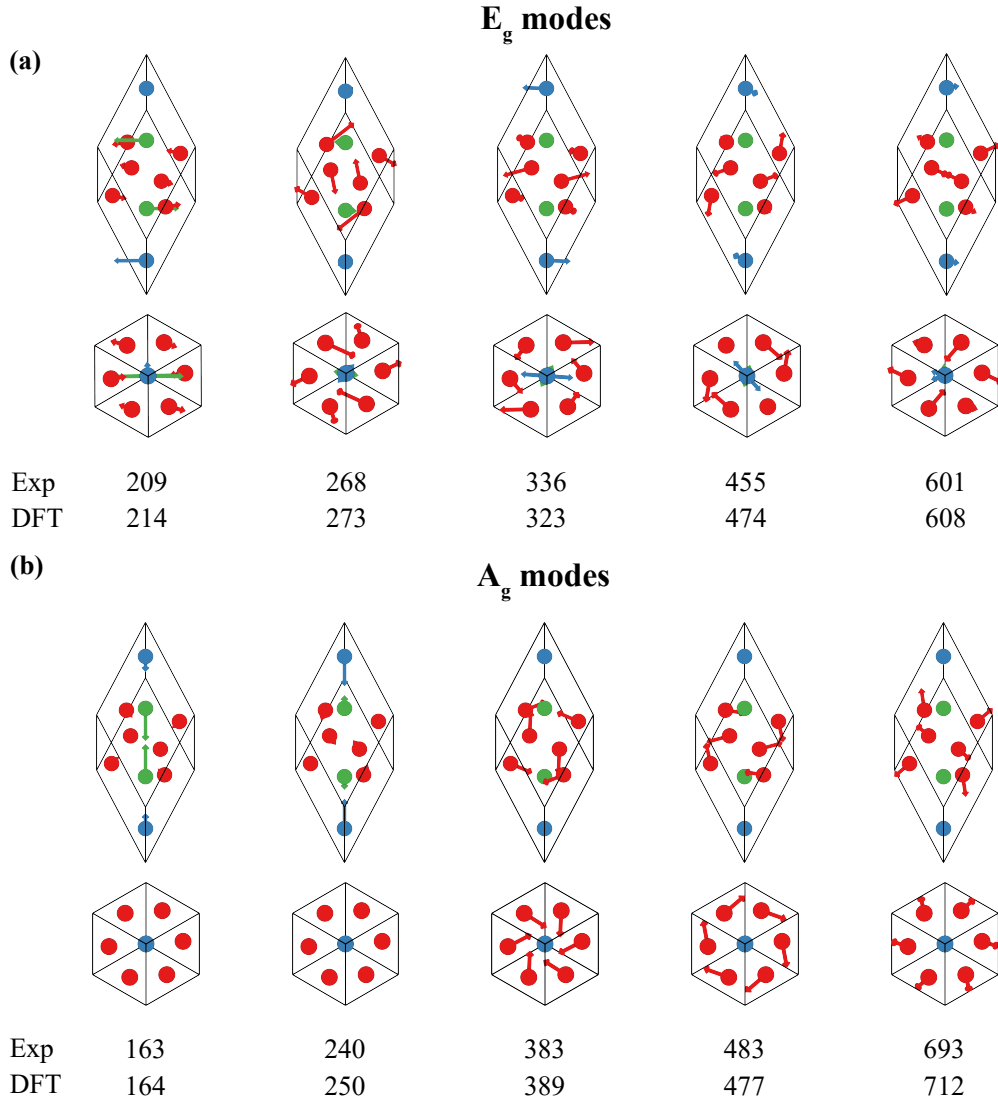


Figure 6: Schematic representation of ionic displacements in the two projections in CoTiO_3 for Raman active (a) $5E_g$ and (b) $5A_g$ phonons in the Brillouin zone center according to the DFT calculations. The relative amplitudes of vibrations are shown by arrows. The experimental and calculated values of phonon frequencies (cm^{-1}) are given.

All even Raman-active modes predicted by symmetry analysis (see Eq. (1)) were observed in the range $150\text{--}800\text{ cm}^{-1}$ with their individual frequencies summarized in Table 2. Generally, the frequencies of these modes are in a good accordance with the results of DFT calculations, however they are slightly softer due to anharmonic effects at finite, room in our experiments, temperature, similar to the case of the polar phonons.

Notably, the phonon of the highest frequency 693 cm^{-1} has strongly asymmetric shape, and can be more or less equally good described by two symmetric or one asymmetric Voigt profiles. In Ref. [31] this asymmetric mode was interpreted as the two separate ones. The shape of this mode is similar in all polarizations, and there is no any additional modes at this energy according to the DFT calculations. It seems unlikely that there is an additional mode with frequency $\approx 711\text{ cm}^{-1}$, e.g., created by two-phonon scattering processes having nearly the same Raman tensor elements responsible

for the 693 cm^{-1} excitation, and therefore we may conclude that its asymmetry is intrinsic.

The $b^*(c'c')b^*$ geometry allows the simultaneous observation of all the even phonon modes with considerable intensity. Having complete information of relative intensity of the modes, the polarized Raman scattering can be regarded as a supplementary tool for the easy and fast orientation of CoTiO_3 .

Figure 6 shows the ionic displacement patterns for $5E_g$ and $5A_g$ Raman active modes in ilmenite CoTiO_3 which are similar to those for isostructural CdTiO_3 [33] and MgTiO_3 [29]. According to symmetry analysis, displacements of Co and Ti ions occur in the ab plane for all E_g modes, while for A_g modes these ions move along the c axis. For the lowest-frequency E_g and A_g phonons the opposite directional displacements of Co ions are significant, as can be seen on the right panels in Fig. 4. The average displacements of Ti ions are predominant for the A_g mode with $j = 2$. It should be

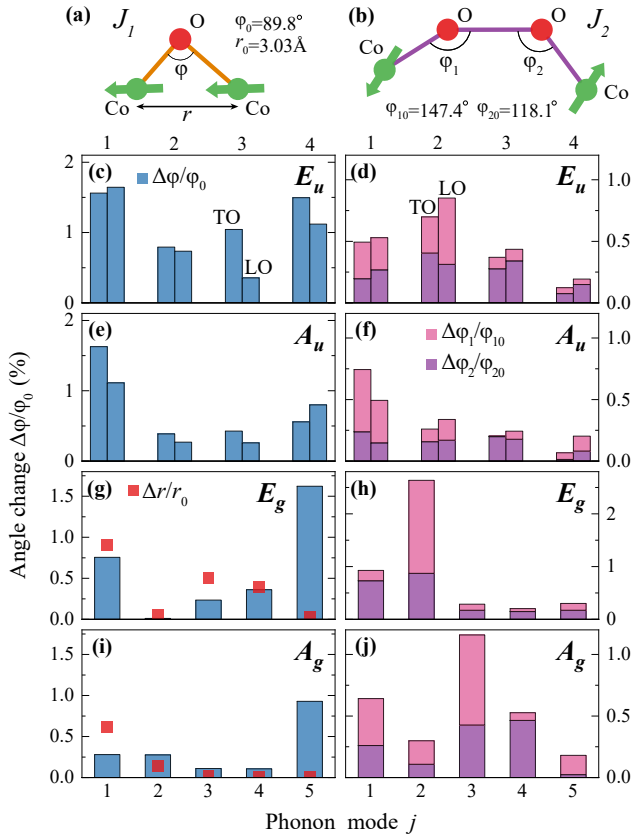


Figure 7: The calculated bond angle changes $\Delta\phi/\phi_0$ of the superexchange (a) J_1 and (b) J_2 interactions due to the ionic displacements for (c,d) E_u , (e,f) A_u , (g,h) E_g and (i,j) A_g optical phonons, respectively. Additionally, Raman active E_g and A_g phonons dynamically change distances $\Delta r/r_0$ of the direct exchange between nearest neighbor Co ions as shown by the red squares. Arrows represent the spin directions. The average values of angles and distance of superexchange paths for both J_1 and J_2 exchange interactions are given.

noted that the A_g modes with $j = 1, 2$ are characterized by relatively small average displacements of O ions as shown in Figs. 4 and 6b. For other A_g modes, the average displacements of Co and Ti ions are relatively small. The displacements of Ti and O ions for E_g phonons are characterized by a non-monotonic dependence on vibrational modes as shown in Fig. 4.

[33]

3.3. Dynamical modulation of the superexchange interactions by phonons

The spin-phonon coupling give rise a numerous intriguing physical phenomena in magnetic materials [52]. This coupling manifest itself in shifts of the phonon frequencies due to magnetic ordering and originates from the modulation of the superexchange integrals by lattice vibrations. It is known that the superexchange interaction strongly depends on the wave function overlap of the electron clouds and, therefore, is extremely sensitive to the relative distances and bond angles between magnetic ions [53, 54]. The DFT calcula-

tions allowed us to estimate the relative magnitude of the dynamical changes of the geometric superexchange paths caused by ionic displacements shown in Figs. 3 and 6. The magnetic structure of ilmenite CoTiO_3 can be adequately described by the two exchange integrals with the values $J_1 = -4.5$ meV and $J_2 = 0.6$ meV [14].

The anisotropic ferromagnetic J_1 interaction within the ab planes is formed by the direct cation-cation exchange coupling between the nearest-neighbor cations and the 90° cation-anion-cation superexchange coupling [55] as shown in Figs. 1b and 7a. The displacements of ions for infrared active E_u and A_u phonons shown in Fig. 3 lead to a dynamic change of the superexchange Co–O–Co bond angles $\Delta\phi/\phi_0$. For Raman active E_g and A_g phonons the vibrations of ions (see Fig. 6), besides the bond angles, also lead to dynamical changes of the relative distance $\Delta r/r_0$ of the direct Co–Co exchange interaction. The isotropic antiferromagnetic superexchange J_2 interaction occurs via next-nearest-neighbor coupling along the cation-anion-anion-cation path in the direction of the c axis [55] as shown in Figs. 1b and 7b. For the J_2 interaction all lattice vibrations dynamically change bond angles ϕ_1 and ϕ_2 of the Co–O–O–Co path only.

Figures 7c–j present the calculated relative changes of angles (bars) and distance (squares) for superexchange J_1 and J_2 interactions for studied phonons. Analysis of the obtained results allows us to predict the relative values of the phonon frequency shifts at antiferromagnetic ordering caused by the spin-phonon coupling. Since the absolute value of J_1 is almost an order of magnitude larger than J_2 , we took into account only the effects of the strongest exchange interaction on the phonon frequencies. We predict that the spin-phonon coupling should manifest itself for polar E_u and A_u phonons proportional to the dynamical modulation of the ϕ angle (see Figs. 7c and d). Furthermore, for the E_u with $j = 3$ phonon the significant spin-phonon coupling is expected for ω_{TO} , while for ω_{LO} this effect is expected to be much weaker. One may expect that a change in the relative distance r between Co–Co ions has a stronger effect on the J_1 interaction than the bond ϕ angle. Thus, the largest frequency shifts are expected for the Raman active E_g and A_g phonons with frequencies 163, 209, 336 and 455 cm^{-1} due to dynamic modulation of the direct distance $\Delta r/r_0$ as shown in Figs. 7g and i. It should be noted that possible deviations between the predicted and experimentally observed phonon frequency shifts may be related to magnetoelastic coupling [56], strong anisotropy of J_1 [14] and effect of J_2 interactions. Nevertheless, all these computational predictions require experimental confirmation.

3.4. Dielectric spectroscopy

Temperature dependencies of the dielectric permittivity and dissipation factor in CoTiO_3 in the temperature range 5–400 K at frequencies from 5 kHz to 1 MHz are shown in Fig. 8. The absolute values of the ϵ_0 were normalized to the corresponding quantities from far-infrared reflectivity. Significant increase of the dielectric permittivity with essential frequency dispersion is observed at high temperatures for

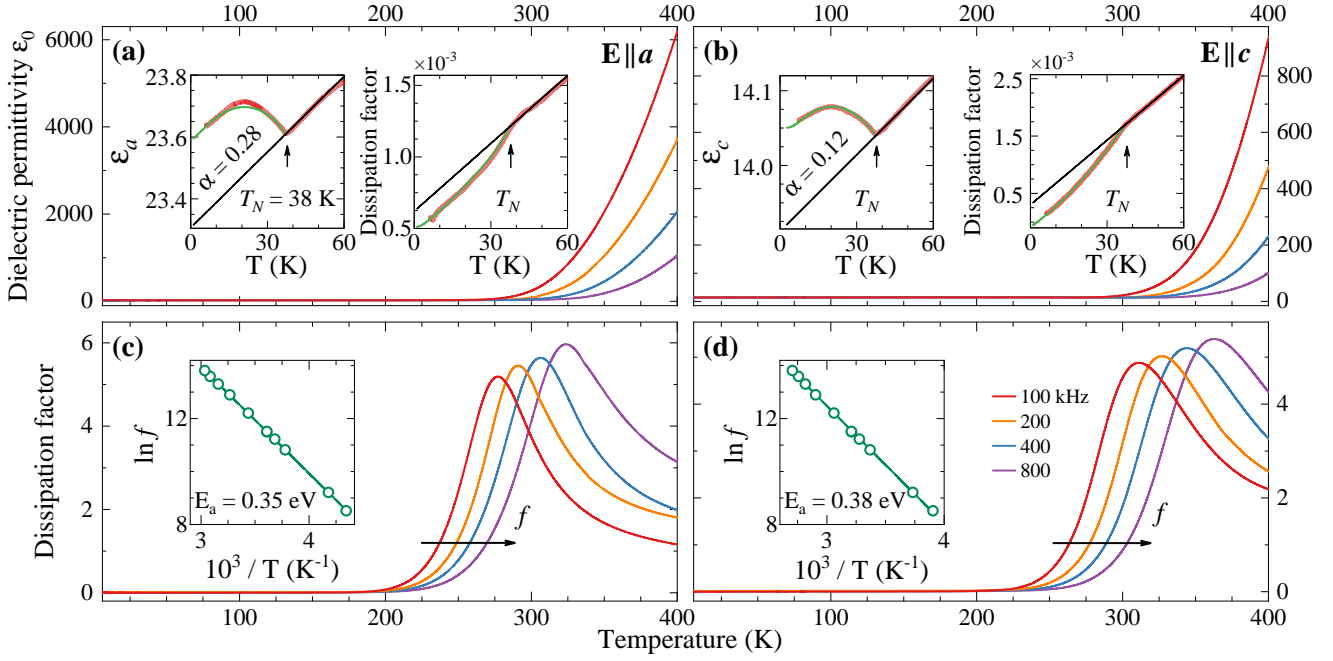


Figure 8: Temperature dependencies of the (a), (b) dielectric permittivity and (c), (d) dissipation factor at the indicated frequencies in CoTiO_3 along the a and c axes, respectively. Insets in (a) and (b) show changes of $\epsilon_0(T)$ at 100 kHz below T_N due to antiferromagnetic ordering for relevant axes. The black lines are the expected behavior of ϵ_0^{NM} assuming absence of antiferromagnetic ordering. The green lines are fits of the shifts due to spontaneous magnetodielectric effect according to Eq. (7). Arrhenius plots obtained from dissipation factor data are shown on insets in (c) and (d) for a and c axes, respectively.

both main axes, as can be seen in Figs. 8a and b. Moreover, the dissipation factor demonstrate peaks in the same temperature range which are also frequency dependent and obey the Arrhenius law $f = f_0 \exp \frac{-E_a}{k_B T}$ as shown on insets in Figs. 8c and d for a and d axes, respectively. The obtained values of activation energy $E_a = 0.35$ and 0.38 eV are close to the those for ceramic sample of CoTiO_3 from Ref. [57]. This relaxation process is apparently due to hopping conductivity [58] which was previously observed in the related inverse spinel Co_2TiO_4 [59] and some other oxide crystals [60, 61, 62].

The distinct anomaly in the temperature dependence of the dielectric permittivity is observed for both a and c axes at $T_N = 38$ K due to the antiferromagnetic ordering, as shown on insets in Figs. 8a and b, respectively. It is interesting to note that in MnTiO_3 which are isostructural but with different magnetic structure the anomalies of the dielectric permittivity below T_N were observed only in an external magnetic field [17]. The expected behavior of the dielectric permittivity ϵ_0^{NM} assuming absence of antiferromagnetic ordering at low temperatures is shown by black lines on insets in Figs. 8a and b. The deviation of $\epsilon_0(T)$ from the expected behavior of $\epsilon_0^{\text{NM}}(T)$ below T_N due to the spontaneous magnetodielectric effect was fitted by expression [63]

$$\Delta\epsilon^{\text{MD}}(T) = \alpha \langle S_i \cdot S_j \rangle, \quad (7)$$

where α is a coefficient and $\langle S_i \cdot S_j \rangle$ is the spin-pair correlation function between nearest-neighbor spins, which was

represented as the squared Brillouin function for simplicity [64]. There is a good agreement between experimental (red) and fit (green) lines on insets in Figs. 8a and b.

Obtained values of spontaneous magnetodielectric effect accounts for about $\alpha = 0.28$ and 0.12 for the a and c axes, respectively. It is worth noting that these values α are comparable in magnitude as those observed in polycrystalline ilmenites CoTiO_3 and NiTiO_3 [16]. However, in our experiments the spontaneous magnetodielectric effect is positive in CoTiO_3 , i.e., it leads to increase of the dielectric permittivity below T_N for the both main crystallographic axes whereas in polycrystalline sample this effect was negative [16]. Moreover, the temperature behavior of $\Delta\epsilon^{\text{MD}}$ in single crystal of CoTiO_3 is similar to that observed in NiTiO_3 with the same crystal and magnetic structures [16].

The spontaneous magnetodielectric effect can be caused by discussed above the dynamical modulation of the exchange interaction by infrared active phonons [65] and by direct crystal volume changes at magnetic ordering due to magnetoelastic coupling [66]. It was suggested that the magnetodielectric effect in ilmenite NiTiO_3 single crystal is mainly related to the magnetoelastic coupling [56]. Also, the spontaneous magnetostriction was experimentally observed in isostructural FeTiO_3 [67]. It is interesting to note that in the related inverse spinel Co_2TiO_4 no anomaly in the temperature dependence of the dielectric permittivity at the ferrimagnetic phase transition was revealed [59]. In our opinion, the observed spontaneous magnetodielectric effect in ilmenite CoTiO_3 has a primarily magnetoelastic origin whereas the

effect of spin-phonon coupling is less pronounced. This suggestion is confirmed by the fact that not only the dielectric permittivity, but also the dissipation factor shows changes due to the antiferromagnetic ordering as can be seen on insets in Figs. 8c and d. Further experimental studies of the lattice dynamics at low temperatures of ilmenite CoTiO_3 could reveal more deep insight into the origin of the magnetodielectric coupling.

4. Conclusions

In summary, we report the results of detailed lattice dynamics studies of cobalt titanite CoTiO_3 single crystal with ilmenite structure using complementary dielectric, far-infrared, and Raman polarized spectroscopic techniques. Obtained experimental results, supplemented by the DFT calculations, allowed us to reliably identify the frequencies and symmetries of all predicted infrared and Raman active phonons. It was shown that the antiferromagnetic ordering is accompanied by changes the low-frequency dielectric permittivity in zero external magnetic field due to the spontaneous magnetodielectric effect. We believe that our results will stimulate further research in deep of CoTiO_3 and other ilmenite-type crystals.

Declaration of competing interest

The authors declare that they have no known competing financial interests or personal relationships that could have appeared to influence the work reported in this paper.

Acknowledgements

We thank D. A. Andronikova and M. P. Scheglov for the help with the X-ray orientation of the single crystal and K. N. Boldyrev for scientific discussion. M. A. P. acknowledges fruitful discussions with Beatrice T. Crow. N. V. S., R. M. D. and R. V. P. are grateful to Russian Science Foundation [project number 16-12-10456] for financial support. Besides, the authors would like to thank the HFML-RU/FOM, a member of the European Magnetic Field Laboratory (EMFL) for support of the Raman spectroscopy study.

CRedit authorship contribution statement

R. M. Dubrovin: Conceptualization, Validation, Formal analysis, Investigation, Writing - Original Draft, Visualization. **N. V. Siverin:** Investigation, Validation, Formal analysis, Visualization. **M. A. Prosnikov:** Validation, Formal analysis, Investigation, Writing - Original Draft, Visualization. **V. A. Chernyshev:** Formal analysis. **N. N. Novikova:** Investigation. **P. C. M. Christianen:** Resources. **A. M. Balbashov:** Resources. **R. V. Pisarev:** Writing - Review & Editing, Supervision, Project administration, Funding acquisition.

References

- [1] R. J. D. Tilley, *Perovskites: Structure-Property Relationships*, John Wiley & Sons, Chichester, West Sussex, UK, 2016.
- [2] T. R. Cunha, A. D. Rodrigues, J. E. Rodrigues, D. V. Sampaio, B. J. A. Moulton, R. C. da Costa, P. S. Pizani, Thermal expansion, compressibility and bulk modulus of ilmenite-type CoTiO_3 : X-ray diffraction at high pressures and temperatures, *Solid State Sci.* 88 (2019) 1–5. doi:10.1016/j.solidstatesciences.2018.12.005. URL <https://doi.org/10.1016/j.solidstatesciences.2018.12.005>
- [3] T.-S. Chao, W.-M. Ku, H.-C. Lin, D. Landheer, Y.-Y. Wang, Y. Mori, CoTiO_3 high- κ dielectrics on HSG for DRAM applications, *IEEE Trans. Electron Devices* 51 (12) (2004) 2200–2204. doi:10.1109/TED.2004.839880. URL <https://doi.org/10.1109/TED.2004.839880>
- [4] U. Ullah, W. F. F. W. Ali, M. F. Ain, N. M. Mahyuddin, Z. A. Ahmad, Design of a novel dielectric resonator antenna using MgTiO_3 - CoTiO_3 for wideband applications, *Mater. Des.* 85 (2015) 396–403. doi:10.1016/j.matdes.2015.07.026. URL <https://doi.org/10.1016/j.matdes.2015.07.026>
- [5] J. H. Hwang, E. N. Son, R. Lee, S. H. Kim, J. I. Baek, H. J. Ryu, K. T. Lee, J. M. Sohn, A thermogravimetric study of CoTiO_3 as oxygen carrier for chemical looping combustion, *Catal. Today* 303 (2018) 13–18. doi:10.1016/j.cattod.2017.09.060. URL <https://doi.org/10.1016/j.cattod.2017.09.060>
- [6] A. V. Agafonov, A. V. Vinogradov, Catalytically active materials based on titanium dioxide: ways of enhancement of photocatalytic activity, *High Energy Chem.* 42 (7) (2008) 578–580. doi:10.1134/S0018143908070242. URL <https://doi.org/10.1134/S0018143908070242>
- [7] M. A. Ehsan, R. Naeem, V. McKee, A. Rehman, A. S. Hakeem, M. Mazhar, Fabrication of photoactive CaTiO_3 - TiO_2 composite thin film electrodes via facile single step aerosol assisted chemical vapor deposition route, *J. Mater. Sci. Mater. Electron.* 30 (2) (2019) 1411–1424. doi:10.1007/s10854-018-0411-4. URL <https://doi.org/10.1007/s10854-018-0411-4>
- [8] M. Siemons, U. Simon, Gas sensing properties of volume-doped CoTiO_3 synthesized via polyol method, *Sens. Actuators, B* 126 (2) (2007) 595–603. doi:10.1016/j.snb.2007.04.009. URL <https://doi.org/10.1016/j.snb.2007.04.009>
- [9] J. Lu, N. Jia, L. Cheng, K. Liang, J. Huang, J. Li, rGO/ CoTiO_3 nanocomposite with enhanced gas sensing performance at low working temperature, *J. Alloys Compd.* 739 (2018) 227–234. doi:10.1016/j.jallcom.2017.12.129. URL <https://doi.org/10.1016/j.jallcom.2017.12.129>
- [10] J. Xu, W. Ding, W. Zhao, W. Zhao, Z. Hong, F. Huang, In situ growth enabling ideal graphene encapsulation upon mesocrystalline MTiO_3 ($M = \text{Ni}, \text{Co}, \text{Fe}$) nanorods for stable lithium storage, *ACS Energy Lett.* 2 (3) (2017) 659–663. doi:10.1021/acsenergylett.7b00018. URL <https://doi.org/10.1021/acsenergylett.7b00018>
- [11] M. Li, X. Xiao, Y. Liu, W. Zhang, Y. Zhang, L. Chen, Ternary perovskite cobalt titanate/graphene composite material as long-term cyclic anode for lithium-ion battery, *J. Alloys Compd.* 700 (2017) 54–60. doi:10.1016/j.jallcom.2017.01.073. URL <https://doi.org/10.1016/j.jallcom.2017.01.073>
- [12] J. Li, D. Wang, J. Zhou, L. Hou, F. Gao, MOF-derived in situ synthesized carbon-coated ilmenite cobalt titanate nanocrystalline, high-stability lithium-ion batteries, *J. Alloys Compd.* 793 (2019) 247–258. doi:10.1016/j.jallcom.2019.04.100. URL <https://doi.org/10.1016/j.jallcom.2019.04.100>
- [13] J. Jiang, J. Luo, J. Zhu, X. Huang, J. Liu, T. Yu, Diffusion-controlled evolution of core-shell nanowire arrays into integrated hybrid nanotube arrays for Li-ion batteries, *Nanoscale* 5 (17) (2013) 8105–8113. doi:10.1039/C3NR01786A. URL <https://doi.org/10.1039/C3NR01786A>
- [14] B. Yuan, I. Khait, G.-J. Shu, F. C. Chou, M. B. Stone, J. P. Clancy, A. Paramekanti, Y.-J. Kim, Dirac magnons in a honeycomb lattice quantum xy magnet CoTiO_3 , *Phys. Rev. X* 10 (2020) 011062. doi:10.1103/PhysRevX.10.011062.

- URL <https://link.aps.org/doi/10.1103/PhysRevX.10.011062>
- [15] M. Elliot, P. A. McClarty, D. Prabhakaran, R. D. Johnson, H. C. Walker, P. Manuel, R. Coldea, Visualization of Isospin Momentum Texture of Dirac Magnons and Excitons in a Honeycomb Quantum Magnet, arXiv preprint arXiv:2007.04199 (2020). URL <https://arxiv.org/abs/2007.04199>
- [16] J. K. Harada, L. Balhorn, J. Hazi, M. C. Kemei, R. Seshadri, Magnetodielectric coupling in the ilmenites MTiO_3 ($M = \text{Co}, \text{Ni}$), Phys. Rev. B 93 (2016) 104404. doi:10.1103/PhysRevB.93.104404. URL <https://link.aps.org/doi/10.1103/PhysRevB.93.104404>
- [17] N. Mufti, G. R. Blake, M. Mostovoy, S. Riyadi, A. A. Nugroho, T. T. M. Palstra, Magnetoelectric coupling in MnTiO_3 , Phys. Rev. B 83 (2011) 104416. doi:10.1103/PhysRevB.83.104416. URL <https://link.aps.org/doi/10.1103/PhysRevB.83.104416>
- [18] H. J. Silverstein, E. Skoropata, P. M. Sarte, C. Mauws, A. A. Aczel, E. S. Choi, J. van Lierop, C. R. Wiebe, H. Zhou, Incommensurate crystal supercell and polarization flop observed in the magnetoelectric ilmenite MnTiO_3 , Phys. Rev. B 93 (2016) 054416. doi:10.1103/PhysRevB.93.054416. URL <https://link.aps.org/doi/10.1103/PhysRevB.93.054416>
- [19] T. Sato, N. Abe, S. Kimura, Y. Tokunaga, T.-h. Arima, Magnetochiral Dichroism in a Collinear Antiferromagnet with No Magnetization, Phys. Rev. Lett. 124 (2020) 217402. doi:10.1103/PhysRevLett.124.217402. URL <https://link.aps.org/doi/10.1103/PhysRevLett.124.217402>
- [20] E. J. Baran, I. L. Botto, Die IR-Spektren einiger Doppeloxide mit Ilmenit-Struktur, Z. Anorg. Allg. Chem. 444 (1) (1978) 282–288. doi:10.1002/zaac.19784440132. URL <https://doi.org/10.1002/zaac.19784440132>
- [21] E. J. Baran, I. L. Botto, Das Infrarotspektrum von Ilmenite, Neus. Jahrb. Mineral. Mh (2) (1981) 56–58.
- [22] O. Yamaguchi, M. Morimi, H. Kawabata, K. Shimizu, Formation and transformation of ZnTiO_3 , J. Am. Ceram. Soc. 70 (5) (1987) C–97. doi:10.1111/j.1151-2916.1987.tb05011.x. URL <https://doi.org/10.1111/j.1151-2916.1987.tb05011.x>
- [23] A. M. Hofmeister, IR reflectance spectra of natural ilmenite; comparison with isostructural compounds and calculation of thermodynamic properties, Eur. J. Mineral. 5 (2) (1993) 281–295. doi:10.1127/ejm/5/2/0281. URL <https://doi.org/10.1127/ejm/5/2/0281>
- [24] C.-H. Wang, X.-J. Kuang, X.-P. Jing, J. Lu, X. Lü, J. Shao, Far infrared reflection spectrum and IR-active modes of MgTiO_3 , J. Appl. Phys. 103 (7) (2008) 074105. doi:10.1063/1.2903913. URL <https://doi.org/10.1063/1.2903913>
- [25] J. E. Rodrigues, M. M. Ferrer, M. L. Moreira, J. R. Sambrano, R. C. Costa, A. D. Rodrigues, P. S. Pizani, Y. Huttel, J. A. Alonso, C. Pecharrmán, Unveiling the infrared complex dielectric function of ilmenite CdTiO_3 , J. Alloys Compd. 813 (2020) 152136. doi:10.1016/j.jallcom.2019.152136. URL <https://doi.org/10.1016/j.jallcom.2019.152136>
- [26] E. J. Baran, I. L. Botto, Die Raman-Spektren von ZnTiO_3 und CdTiO_3 , Z. Anorg. Allg. Chem. 448 (1) (1979) 188–192. doi:10.1002/zaac.19794480123. URL <https://doi.org/10.1002/zaac.19794480123>
- [27] J. Ko, N. E. Brown, A. Navrotsky, C. T. Prewitt, T. Gasparik, Phase equilibrium and calorimetric study of the transition of MnTiO_3 from the ilmenite to the lithium niobate structure and implications for the stability field of perovskite, Phys. Chem. Miner. 16 (8) (1989) 727–733. doi:10.1007/BF00209693. URL <https://doi.org/10.1007/BF00209693>
- [28] M. I. Baraton, G. Busca, M. C. Prieto, G. Ricchiardi, V. S. Escribano, On the vibrational spectra and structure of FeCrO_3 and of the ilmenite-type compounds CoTiO_3 and NiTiO_3 , J. Solid State Chem. 112 (1) (1994) 9–14. doi:10.1006/jssc.1994.1256. URL <https://doi.org/10.1006/jssc.1994.1256>
- [29] C.-H. Wang, X.-P. Jing, W. Feng, J. Lu, Assignment of Raman-active vibrational modes of MgTiO_3 , J. Appl. Phys. 104 (3) (2008) 034112. doi:10.1063/1.2966717. URL <https://doi.org/10.1063/1.2966717>
- [30] X. Wu, S. Qin, L. Dubrovinsky, Investigation into high-pressure behavior of MnTiO_3 : X-ray diffraction and Raman spectroscopy with diamond anvil cells, Geosci. Front. 2 (1) (2011) 107–114. doi:10.1016/j.gsf.2010.09.003. URL <https://doi.org/10.1016/j.gsf.2010.09.003>
- [31] Y. Fujioka, J. Frantti, A. Puretzy, G. King, Raman Study of the Structural Distortion in the $\text{Ni}_{1-x}\text{Co}_x\text{TiO}_3$ Solid Solution, Inorg. Chem. 55 (18) (2016) 9436–9444. doi:10.1021/acs.inorgchem.6b01693. URL <https://doi.org/10.1021/acs.inorgchem.6b01693>
- [32] A. Sakai, G. Anzou, A. Kikuchi, O. Seri, Raman scattering study of microcrystals of perovskite titanates, Ferroelectrics 512 (1) (2017) 45–51. doi:10.1080/00150193.2017.1355159. URL <https://doi.org/10.1080/00150193.2017.1355159>
- [33] J. E. Rodrigues, M. M. Ferrer, T. R. Cunha, R. C. Costa, J. R. Sambrano, A. D. Rodrigues, P. S. Pizani, First-principles calculations and Raman scattering evidence for local symmetry lowering in rhombohedral ilmenite: temperature- and pressure-dependent studies, J. Phys.: Condens. Matter 30 (48) (2018) 485401. doi:10.1088/1361-648X/aae803. URL <https://doi.org/10.1088/1361-648X/aae803>
- [34] A. M. Balbashov, A. A. Mukhin, V. Y. Ivanov, L. D. Iskhakova, M. E. Voronchikhina, Electric and magnetic properties of titanium-cobalt-oxide single crystals produced by floating zone melting with light heating, Low Temp. Phys. 43 (8) (2017) 965–970. doi:10.1063/1.5001297. URL <https://link.aps.org/doi/10.1063/1.5001297>
- [35] A. D. Becke, Density-functional thermochemistry. III. The role of exact exchange, J. Chem. Phys. 98 (7) (1993) 5648–5652. doi:10.1063/1.464913. URL <https://doi.org/10.1063/1.464913>
- [36] R. Dovesi, R. Orlando, A. Erba, C. M. Zicovich-Wilson, B. Civalleri, S. Casassa, L. Maschio, M. Ferrabone, M. De La Pierre, P. d'Arco, et al., CRYSTAL14: A program for the *ab initio* investigation of crystalline solids, Int. J. Quantum Chem. 114 (19) (2014) 1287–1317. doi:10.1002/qua.24658. URL <https://doi.org/10.1002/qua.24658>
- [37] M. F. Peintinger, D. V. Oliveira, T. Bredow, Consistent gaussian basis sets of triple-zeta valence with polarization quality for solid-state calculations, J. Comput. Chem. 34 (6) (2013) 451–459. doi:10.1002/jcc.23153. URL <https://doi.org/10.1002/jcc.23153>
- [38] G. Sophia, P. Baranek, C. Sarrazin, M. Rérat, R. Dovesi, First-principles study of the mechanisms of the pressure-induced dielectric anomalies in ferroelectric perovskites, Phase Transit. 86 (11) (2013) 1069–1084. doi:10.1080/01411594.2012.754442. URL <https://doi.org/10.1080/01411594.2012.754442>
- [39] N. N. Kuzmin, S. A. Klimin, B. N. Mavrin, K. N. Boldyrev, V. A. Chernyshev, B. V. Mill, M. N. Popova, Lattice dynamics and structure of the new langasite $\text{Ln}_3\text{CrGe}_3\text{Be}_2\text{O}_{14}$ ($\text{Ln} = \text{La}, \text{Pr}, \text{Nd}$): vibrational spectra and *ab initio* calculations, J. Phys. Chem. Solids 138 (2020) 109266.
- [40] L. Maschio, B. Kirtman, R. Orlando, M. Rérat, *Ab initio* analytical infrared intensities for periodic systems through a coupled perturbed Hartree-Fock/Kohn-Sham method, J. Chem. Phys. 137 (20) (2012) 204113. doi:10.1063/1.4767438. URL <https://doi.org/10.1063/1.4767438>
- [41] L. Maschio, B. Kirtman, M. Rérat, R. Orlando, R. Dovesi, *Ab initio* analytical Raman intensities for periodic systems through a coupled perturbed Hartree-Fock/Kohn-Sham method in an atomic orbital basis. I. Theory, J. Chem. Phys. 139 (16) (2013) 164101. doi:10.1063/1.4824442. URL <https://doi.org/10.1063/1.4824442>
- [42] K. Momma, F. Izumi, VESTA 3 for three-dimensional visualization of crystal, volumetric and morphology data, J. Appl. Crystallogr. 44 (6) (2011) 1272–1276. doi:10.1107/S0021889811038970. URL <https://doi.org/10.1107/S0021889811038970>
- [43] R. E. Newnham, J. H. Fang, R. P. Santoro, Crystal structure and

- magnetic properties of CoTiO_3 , *Acta Cryst.* 17 (3) (1964) 240–242. doi:10.1107/S0365110X64000615.
URL <https://doi.org/10.1107/S0365110X64000615>
- [44] K. T. Jacob, G. Rajitha, Role of entropy in the stability of cobalt titanates, *J. Chem. Thermodyn.* 42 (7) (2010) 879–885. doi:10.1016/j.jct.2010.02.016.
URL <https://doi.org/10.1016/j.jct.2010.02.016>
- [45] E. Kroumova, M. I. Aroyo, J. M. Perez-Mato, A. Kirov, C. Capillas, S. Ivantchev, H. Wondratschek, Bilbao crystallographic server: useful databases and tools for phase-transition studies, *Phase Transit.* 76 (1–2) (2003) 155–170.
- [46] F. Gervais, B. Piriou, Anharmonicity in several-polar-mode crystals: adjusting phonon self-energy of LO and TO modes in Al_2O_3 and TiO_2 to fit infrared reflectivity, *J. Phys. C* 7 (13) (1974) 2374. doi:10.1088/0022-3719/7/13/017.
URL <https://doi.org/10.1088/0022-3719/7/13/017>
- [47] M. Born, E. Wolf, *Principles of optics: electromagnetic theory of propagation, interference and diffraction of light*, Elsevier, 2013.
- [48] F. Gervais, H. Arend, Long-wavelength phonons in the four phases of $\{\text{N}(\text{CH}_3)_4\}_2\text{CuCl}_4$ and effective charges, *Z. Phys. B* 50 (1) (1983) 17–22. doi:10.1007/BF01307221.
URL <https://link.springer.com/article/10.1007/BF01307221>
- [49] M. Balkanski, R. F. Wallis, E. Haro, Anharmonic effects in light scattering due to optical phonons in silicon, *Phys. Rev. B* 28 (1983) 1928–1934. doi:10.1103/PhysRevB.28.1928.
URL <https://link.aps.org/doi/10.1103/PhysRevB.28.1928>
- [50] K. Persson, Materials Data on FeTiO_3 (SG:148) by Materials Project, an optional note (11 2014). doi:10.17188/1194428.
- [51] K. Persson, Materials Data on MgTiO_3 (SG:148) by Materials Project, an optional note (7 2014). doi:10.17188/1207400.
- [52] J. Son, B. C. Park, C. H. Kim, H. Cho, S. Y. Kim, L. J. Sandilands, C. Sohn, J.-G. Park, S. J. Moon, T. W. Noh, Unconventional spin-phonon coupling via the Dzyaloshinskii–Moriya interaction, *npj Quantum Mater.* 4 (1) (2019) 1–8. doi:10.1038/s41535-019-0157-0.
URL <https://doi.org/10.1038/s41535-019-0157-0>
- [53] E. Granado, A. García, J. A. Sanjurjo, C. Rettori, I. Torriani, F. Prado, R. D. Sánchez, A. Caneiro, S. B. Oseroff, Magnetic ordering effects in the Raman spectra of $\text{La}_{1-x}\text{Mn}_{1-x}\text{O}_3$, *Phys. Rev. B* 60 (1999) 11879–11882. doi:10.1103/PhysRevB.60.11879.
URL <https://link.aps.org/doi/10.1103/PhysRevB.60.11879>
- [54] S. V. Streltsov, D. I. Khomskii, Orbital physics in transition metal compounds: new trends, *Phys.-Usp.* 60 (11) (2017) 1121. doi:10.3367/UFNe.2017.08.038196.
URL <https://doi.org/10.3367/UFNe.2017.08.038196>
- [55] J. B. Goodenough, J. J. Stickler, Theory of the magnetic properties of the ilmenites MnTiO_3 , *Phys. Rev.* 164 (2) (1967) 768. doi:10.1103/PhysRev.164.768.
URL <https://link.aps.org/doi/10.1103/PhysRev.164.768>
- [56] K. Dey, S. Sauerland, J. Werner, Y. Skourski, M. Abdel-Hafiez, R. Bag, S. Singh, R. Klingeler, Magnetic phase diagram and magnetoelastic coupling of NiTiO_3 , *Phys. Rev. B* 101 (2020) 195122. doi:10.1103/PhysRevB.101.195122.
URL <https://link.aps.org/doi/10.1103/PhysRevB.101.195122>
- [57] T. Acharya, R. N. P. Choudhary, Structural, dielectric and impedance characteristics of CoTiO_3 , *Mater. Chem. Phys.* 177 (2016) 131–139. doi:10.1016/j.matchemphys.2016.04.005.
URL <https://doi.org/10.1016/j.matchemphys.2016.04.005>
- [58] S. R. Elliott, A.c. conduction in amorphous chalcogenide and pnictide semiconductors, *Adv. Phys.* 36 (2) (1987) 135–217. doi:10.1080/00018738700101971.
URL <https://doi.org/10.1080/00018738700101971>
- [59] M. A. Prosnikov, A. D. Molchanova, R. M. Dubrovin, K. N. Boldyrev, A. N. Smirnov, V. Y. Davydov, A. M. Balbashov, M. N. Popova, R. V. Pisarev, Lattice dynamics and electronic structure of cobalt–titanium spinel Co_2TiO_4 , *Phys. Solid State* 58 (12) (2016) 2516–2522. doi:10.1134/S1063783416120258.
URL <https://doi.org/10.1134/S1063783416120258>
- [60] C. Kant, T. Rudolf, F. Schrettle, F. Mayr, J. Deisenhofer, P. Lunkenheimer, M. V. Eremin, A. Loidl, Optical spectroscopy in CoO : Phononic, electric, and magnetic excitation spectrum within the charge-transfer gap, *Phys. Rev. B* 78 (2008) 245103. doi:10.1103/PhysRevB.78.245103.
URL <https://link.aps.org/doi/10.1103/PhysRevB.78.245103>
- [61] M. Savinov, V. A. Trepakov, P. P. Syrnikov, V. Železný, J. Pokorný, A. Dejneka, L. Jastrabik, P. Galinetto, Dielectric properties of Mn doped SrTiO_3 , *J. Phys.: Condens. Matter* 20 (9) (2008) 095221. doi:10.1088/0953-8984/20/9/095221.
URL <https://doi.org/10.1088/0953-8984/20/9/095221>
- [62] K. K. Bamzai, V. Gupta, P. N. Kotru, B. M. Wanklyn, Dielectric and ac conductivity behaviour of flux grown nickel titanate (NiTiO_3) crystal, *Ferroelectrics* 413 (1) (2011) 328–341. doi:10.1080/00150193.2011.531217.
URL <https://doi.org/10.1080/00150193.2011.531217>
- [63] T. Katsufuji, H. Takagi, Coupling between magnetism and dielectric properties in quantum paraelectric EuTiO_3 , *Phys. Rev. B* 64 (2001) 054415. doi:10.1103/PhysRevB.64.054415.
URL <https://link.aps.org/doi/10.1103/PhysRevB.64.054415>
- [64] M. I. Darby, Tables of the brillouin function and of the related function for the spontaneous magnetization, *Br. J. Appl. Phys.* 18 (10) (1967) 1415. doi:10.1088/0508-3443/18/10/307.
URL <https://doi.org/10.1088/0508-3443/18/10/307>
- [65] R. M. Dubrovin, N. V. Siverin, P. P. Syrnikov, N. N. Novikova, K. N. Boldyrev, R. V. Pisarev, Lattice dynamics and microscopic mechanisms of the spontaneous magnetodielectric effect in the antiferromagnetic fluoroperovskites KCoF_3 and RbCoF_3 , *Phys. Rev. B* 100 (2019) 024429. doi:10.1103/PhysRevB.100.024429.
URL <https://link.aps.org/doi/10.1103/PhysRevB.100.024429>
- [66] Y. M. Xie, C. S. Lin, H. Zhang, W. D. Cheng, Magnetodielectric and magnetoelastic coupling in $\text{Co}_4\text{Nb}_2\text{O}_9$ below Néel temperature, *AIP Adv.* 6 (4) (2016) 045006. doi:10.1063/1.4947074.
URL <https://doi.org/10.1063/1.4947074>
- [67] M. Charilaou, D. Sheptyakov, J. F. Löffler, A. U. Gehring, Large spontaneous magnetostriction in FeTiO_3 and adjustable magnetic configuration in Fe(III)-doped FeTiO_3 , *Phys. Rev. B* 86 (2012) 024439. doi:10.1103/PhysRevB.86.024439.
URL <https://link.aps.org/doi/10.1103/PhysRevB.86.024439>